Research articles

Exploiting symmetries in skyrmionic micromagnetic simulations: Cylindrical and radial meshes

Josep Castell-Queralt, Leonardo González-Gómez, Nuria Del-Valle, Carles Navau *

Departament de Física, Universitat Autònoma de Barcelona, Edifici C (campus UAB), 08193 Bellaterra, Barcelona, Catalonia, Spain

ARTICLE INFO

ABSTRACT

Micromagnetic simulations are an essential tool in the theoretical study of magnetic skyrmions. When confined into nanometric samples, these structures can serve as bits of information among other possible applications. Accurate simulations are one of the major sources of theoretical results. In the case of confined skyrmions, it is known that the boundaries play a critical role in their stabilization. However, most of the micromagnetic simulations are done using a finite-difference method with quadrilateral meshes, that do not exactly fit the boundaries. The use of this mesh can introduce a significant numerical error that can completely change the results of the simulations. We present here two different finite-difference meshes to study skyrmions in confined disks, taking advantage of the symmetry of that geometry. A two-dimensional cylindrical mesh for non-symmetric scenarios but geometrically symmetric (boundary conditions) that reduces the propagation of the numerical error, and the particular case of a one dimensional mesh for axisymmetric scenarios where the computation time is hugely reduced.

1. Introduction

Ferromagnetic materials are at the core of a large and diverse number of devices. Besides their description at macroscopic scales, at the submicrometer scale, the magnetization dynamics of these materials is usually modeled using micromagnetics. This model accounts for the dynamics of the local magnetization function, that represents the average of atomic interacting magnetic moments [1–4].

The micromagnetic model has been (and is currently being) used to simulate systems ranging from nanomagnetic data storage [5–7], spintronic logic devices [8,9], or sensors [10,11]. Devices based on skyrmions and other skyrmionic structures are not an exception. Many important advances in their study have been done after micromagnetic calculations (for example, [12–15]). In the case of skyrmions in thin films, they are usually stabilized thanks to the interfacial Dzyaloshinskii–Moriya interaction (iDMI) appearing at the contact surface with a heavy-metal substrate [16]. iDMI is added to the exchange, the anisotropy, the dipolar interaction and, eventually, to the interaction with external fields (or, in general, to other external agents). Moreover, if the skyrmion is confined, the presence of the iDMI, imposes extra restrictions to the equilibrium magnetization distribution [17]. The use of skyrmions in confined geometries has been proposed as elements for magnetic memories in bit patterned recording media or for artificial neural network computation [18,19], among others.

Within the micromagnetic model, the ferromagnet is described by a continuous magnetization field, $\mathbf{M}(\mathbf{r}, t)$ ($\mathbf{r}$ is the position and t the time). This magnetization varies in time due to an effective magnetic field, $\mathbf{H}_{\text{eff}}(\mathbf{r}, t)$, which is not only produced by external sources but also by internal interactions and, thus, depends on the magnetization function itself. The magnetization dynamics is described by the Landau–Lifshitz–Gilbert (LLG) equation [20],

$$(1 + \alpha^2)\frac{d\mathbf{M}}{dt} = -\gamma\mathbf{M} \times \mathbf{H}_{\text{eff}} - \frac{\alpha\gamma}{M_s}\mathbf{M} \times \mathbf{M} \times \mathbf{H}_{\text{eff}}, \qquad (1)$$

where α is the Gilbert damping parameter, γ is the gyromagnetic ratio, and $|\mathbf{M}| = M_s$ is the saturation magnetization, which is assumed to be independent of position and time.

We shall show that in a circular disk and starting from a cylindrically symmetric equilibrium magnetization distribution, like a skyrmion, the time dependent $\mathbf{M}(\mathbf{r}, t)$ evolving according to the LLG equation should preserve this symmetry (if the external field has also that same symmetry). However, when solving numerically the LLG equation with quadrilateral meshes (QM) but having rounded boundaries results in inevitable numerical errors. These errors, usually larger at the boundaries, can affect the whole sample. Refining the meshes to retain the symmetry for short enough calculation times is a valid strategy but at the price of increasing the calculation time.

---

* Corresponding author.
  E-mail address: carles.navau@uab.cat (C. Navau).

Here we propose the use of cylindrical meshes (CM) in skyrmionic micromagnetic simulations in two-dimensional disks in order to reduce the numerical errors triggered by the usual use of rectangular discretizations, without compromising (even increasing) the performance of the calculation in terms of computation time and accuracy. In the case of skyrmions confined in disks, the boundary conditions are determined by the iDMI, which is also the interaction responsible of their stabilization [17,18]. In that case, larger numerical errors at borders could be critical for the validity of the simulation.

We shall proceed as follows. In Section 2, we present the general geometry, boundaries and effective fields used in the calculations and in the problem definition. After some general comments on the error propagation due to quadrilateral meshes with cylindrical boundary conditions (Section 3), we introduce (Section 4) the two-dimensional CM for the cases where the boundaries are axisymmetric but $\mathbf{M}(\mathbf{r}, t)$ is not. The use of this mesh reduces the numerical error and, more importantly, avoids the appearance of erroneously computed metastable magnetic structures due to the $\pi/4$-symmetry of a QM in a circular boundary, as we will show in Section 5. Next, in Section 6, we adapt the study to the case of rings with a central hole, where the roundness of the boundaries have more influence. As a particularly interesting case, we shall also introduce, in Section 7 a variation of the CM to a one-dimensional mesh with cylindrical symmetry for the cases where both, $\mathbf{M}$ and the boundaries are axisymmetric. We finish with the conclusions (Section 8).

2. Geometry, effective fields, and boundaries

We consider a planar ferromagnetic disk of radius R and thickness t_{FM}. We assume that $t_{FM} \ll R$ so that the magnetization and any other magnetic quantity are uniform across the thickness. The problem is thus reduced to a two-dimensional problem. The disk is located on the xy-plane with the center at the origin of coordinates. To fix the notation, we will use both standard Cartesian coordinates (x, y, z) and cylindrical coordinates (ρ, φ, z), with the components of the vectors in these coordinate systems indicated by the corresponding subscript.

We consider here that the effective fields acting on the ferromagnet are the exchange field $\mathbf{H}_A$, the anisotropy field $\mathbf{H}_K$, the iDMI field $\mathbf{H}_D$, and an externally applied field $\mathbf{H}_{\text{ext}}$. Physically, we consider that the ferromagnet is on top of a heavy metal that produces iDMI which not only affects the effective field but also the boundary conditions. We also consider uniaxial anisotropy with the easy axis perpendicular to the disk plane (in the z-direction). Since we consider ultra-thin disks, the demagnetization field is included into the anisotropy field by renormalizing the anisotropy constant [21]. This assumption is valid as long as the sample is an ultrathin film, since in this case the z component of the demagnetizing field is approximately proportional to the z component of the local magnetization, justifying the renormalization. Although the numerical treatment we present would be also valid for other sets of effective fields that could appear considering bulk materials or non-uniaxial anisotropies, we focus on this particular case because it is the usual way for studying skyrmionic structures in thin films. Extensions considering other types of effective fields would be straightforward.

Indeed, the total effective field is expressed as

$$\mathbf{H}_{\text{eff}} = \mathbf{H}_A + \mathbf{H}_K + \mathbf{H}_D + \mathbf{H}_{\text{ext}} =$$
$$= \frac{2A}{\mu_0 M_s^2} \nabla^2 \mathbf{M} + \frac{2K}{\mu_0 M_s^2} M_z \hat{\mathbf{z}} + \frac{2D}{\mu_0 M_s^2} \left[(\nabla \cdot \mathbf{M})\hat{\mathbf{z}} - \nabla M_z \right] + \mathbf{H}_{\text{ext}}, \quad (2)$$

where the terms in the second line are expressed in the same order as in the first one. A is the exchange constant, K the effective uniaxial anisotropy constant, D the iDM constant, and μ_0 the vacuum permeability.

In order to work with non-dimensional magnitudes, we normalize the magnetization and all the fields with respect to M_s, the length

dimensions with respect to the exchange length, $l_{ex} = \sqrt{2A/\mu_0 M_s^2}$, and the time with respect to $(\gamma M_s)^{-1}$. Thus, we define

$$\mathbf{h}_\beta = \frac{\mathbf{H}_\beta}{M_s}, \quad (3)$$

$$\mathbf{m} = \frac{\mathbf{M}}{M_s}, \quad (4)$$

$$\tau = \frac{t}{(\gamma M_s)}, \quad (5)$$

$$\kappa = \frac{2K}{\mu_0 M_s^2}, \quad (6)$$

$$\xi = \frac{l_{ex} D}{A}, \quad (7)$$

where β stands for ext, A, D, K, or eff. The normalized effective field is rewritten as (note that the ∇ operator is now also a normalized operator, which means that the derivatives are done with respect to normalized magnitudes)

$$\mathbf{h}_{\text{eff}} = \nabla^2 \mathbf{m} + \kappa m_z \hat{\mathbf{z}} + \xi \left[(\nabla \cdot \mathbf{m})\hat{\mathbf{z}} - \nabla m_z \right] + \mathbf{h}_{\text{ext}}, \quad (8)$$

and the normalized LLG equation becomes

$$(1 + \alpha^2)\frac{d\mathbf{m}}{d\tau} = -\mathbf{m} \times \mathbf{h}_{\text{eff}} - \alpha \mathbf{m} \times \mathbf{m} \times \mathbf{h}_{\text{eff}}. \quad (9)$$

When considering a circular dot geometry (with radius R) and iDMI, we solve Eq. (9) with boundary condition [17]

$$\left. \frac{\partial \mathbf{m}}{\partial \rho'} \right|_{R'} = \frac{\xi}{2}(\hat{\mathbf{z}} \times \hat{\boldsymbol{\rho}}) \times \mathbf{m}, \quad (10)$$

where $\rho' = \rho/l_{ex}$ and $R' = R/l_{ex}$. For all the examples in this work we have used the following parameters: $l_{ex} = 8.42$ nm, $(\gamma M_s)^{-1} = 7.84$ ps, $\xi = 1.85$, $\kappa = 0.3$, and $\alpha = 0.3$, which are in the range of the common micromagnetic parameters for skyrmionic systems [12,22]. From now, and for the rest of the paper, although we will not explicitly write it, all the magnitudes are considered as *normalized* magnitudes, including coordinates. To simplify notation, we will skip the primes in ρ' and R'.

3. General considerations on the symmetry of the solutions

Given Eqs. (8), (9), and (10) in a circular dot, one sees that if both the initial magnetization distribution and the external field are axisymmetric, $\mathbf{m}(\mathbf{r}, \tau = 0) = \mathbf{m}(\rho, \tau = 0)$, and $\mathbf{h}_{\text{ext}}(\mathbf{r}, \tau = 0) = \mathbf{h}_{\text{ext}}(\rho, \tau = 0)$, then the initial effective field also shares the same symmetry: $\mathbf{h}_{\text{eff}}(\mathbf{r}, \tau = 0) = \mathbf{h}_{\text{eff}}(\rho, \tau = 0)$. If both initial $\mathbf{m}$ and $\mathbf{h}_{\text{eff}}$ are axisymmetric, it follows that $\mathbf{m} \times \mathbf{h}_{\text{eff}}$ and $\mathbf{m} \times (\mathbf{m} \times \mathbf{h}_{\text{eff}})$ are also axisymmetric. Hence, according to Eq. (9), the initial variation over time of the magnetization should also be axisymmetric: $\frac{d\mathbf{m}}{d\tau}(\mathbf{r}, \tau = 0) = \frac{d\mathbf{m}}{d\tau}(\rho, \tau = 0)$. Finally, if both the magnetization and its time derivative have radial symmetry, then this symmetry should be conserved over time: $\mathbf{m}(\mathbf{r}, \tau) = \mathbf{m}(\rho, \tau)$.

In summary, in a ferromagnetic ultra-thin dot, if we initially have an axisymmetric magnetic structure and we apply an axisymmetric external field, the structure can evolve in time, but it must conserve the symmetry all the time.

However, when solving the LLG using finite differences in a QM we shall show that, even though initially both the initial magnetization and the applied field are axially symmetric, one could obtain structures that do not conserve the axial symmetry. As an example, consider a ferromagnetic dot of radius R, with an initial magnetization distribution as follows:

$$m_\rho = \sin\left(\frac{\xi\rho}{2}\right), \quad (11)$$

$$m_\varphi = 0, \quad (12)$$

$$m_z = \cos\left(\frac{\xi\rho}{2}\right). \quad (13)$$

This initial magnetization satisfies the boundary conditions, Eq. (10). We can compute the effective fields ($\mathbf{h}_{\text{ext}} = 0$), obtaining

$$h_{\text{eff},\rho} = \left(\frac{\xi^2}{4} - \frac{1}{\rho^2} \right) \sin\left(\frac{\xi\rho}{2} \right) + \frac{\xi}{2} \cos\left(\frac{\xi\rho}{2} \right), \quad (14)$$
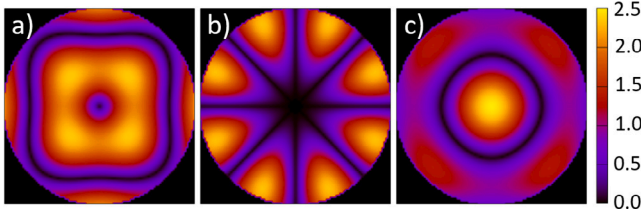
Fig. 1. Difference between the effective field components multiplied by 10^3 [(a): radial, (b): angular, and (c): axial] when calculated numerically using a QM (square-shaped cells of side $R/100$) and when evaluated with the analytical expressions of Eqs. (14)–(16).

$$h_{\text{eff},\varphi} = 0, \tag{15}$$

$$h_{\text{eff},z} = \frac{\xi}{2\rho} \sin\left(\frac{\xi\rho}{2}\right) + \frac{\xi^2}{4} \cos\left(\frac{\xi\rho}{2}\right). \tag{16}$$

In Fig. 1 we show the difference between the numerically calculated effective field using a QM and the effective field analytically obtained from Eqs. (14)–(16), considering the same magnetization distributions given in Eqs. (11)–(13). It is clear that there is a slight difference between both but the interesting part is that the symmetry of that numerical difference is not cylindrical but it has a $\pi/4$-rotation symmetry. That slight difference will produce, following the numerical time integration of Eq. (9), a (numerically) non-symmetric magnetization distribution. At each time step this numerical error propagates with the possible appearance of magnetic structures with a rotation symmetry of $\pi/4$ or $\pi/2$, the same symmetries than the error distribution and the QM have.

The numerical error produced by the QM is higher at the boundaries, due to the fact that the boundary cannot be exactly fitted. This error is specially relevant when iDM interaction is present since it affects not only to the effective field but also directly to the boundary conditions. In materials with larger ξ (large iDM constant) we have steeper space derivatives at the boundaries [Eq. (10)] and thus, since the numerical error using finite differences is proportional to the spatial derivatives, larger numerical errors with the QM mesh.

4. The cylindrical mesh, CM

In order to precisely simulate skyrmionic structures confined in dots, we propose a new type of mesh which, without being fully axially symmetric, takes advantage of the cylindrical symmetry.

It is important to note that, while the introduced CM is axisymmetric, neither the applied field nor the magnetization distribution need to be cylindrically symmetric.

The effective fields, expressed in standard cylindrical coordinates (ρ, φ, z), can be expressed as:

$$\mathbf{h}_A = \left(\frac{\partial^2 m_\rho}{\partial \rho^2} + \frac{1}{\rho} \frac{\partial m_\rho}{\partial \rho} - \frac{m_\rho}{\rho^2} + \frac{1}{\rho^2} \frac{\partial^2 m_\rho}{\partial \varphi^2} - \frac{2}{\rho^2} \frac{\partial m_\varphi}{\partial \varphi} \right) \hat{\boldsymbol{\rho}} +$$
$$+ \left(\frac{\partial^2 m_\varphi}{\partial \rho^2} + \frac{1}{\rho} \frac{\partial m_\varphi}{\partial \rho} - \frac{m_\varphi}{\rho^2} + \frac{1}{\rho^2} \frac{\partial^2 m_\varphi}{\partial \varphi^2} - \frac{2}{\rho^2} \frac{\partial m_\rho}{\partial \varphi} \right) \hat{\boldsymbol{\varphi}} +$$
$$+ \left(\frac{\partial^2 m_z}{\partial \rho^2} + \frac{1}{\rho} \frac{\partial m_z}{\partial \rho} + \frac{1}{\rho^2} \frac{\partial^2 m_z}{\partial \varphi^2} \right) \hat{\mathbf{z}}, \tag{17}$$

$$\mathbf{h}_D = \xi \left[-\frac{\partial m_z}{\partial \rho} \hat{\boldsymbol{\rho}} + \frac{1}{\rho} \frac{\partial m_\varphi}{\partial \varphi} \hat{\boldsymbol{\varphi}} + \frac{1}{\rho} \left(m_\rho + \rho \frac{\partial m_\rho}{\partial \rho} + \frac{\partial m_\varphi}{\partial \varphi} \right) \hat{\mathbf{z}} \right], \tag{18}$$

$$\mathbf{h}_K = \kappa m_z \hat{\mathbf{z}}, \tag{19}$$

$$\mathbf{h}_{\text{ext}} = h_{\text{ext}} \hat{\mathbf{z}}. \tag{20}$$

The proposed mesh is sketched in Fig. 2, compared with the standard QM. Note that the CM has uniform radial discretization step but adaptative angular discretization step (depending on the radial distance). The mesh is constructed using the following algorithm. Given a disk of radius R:
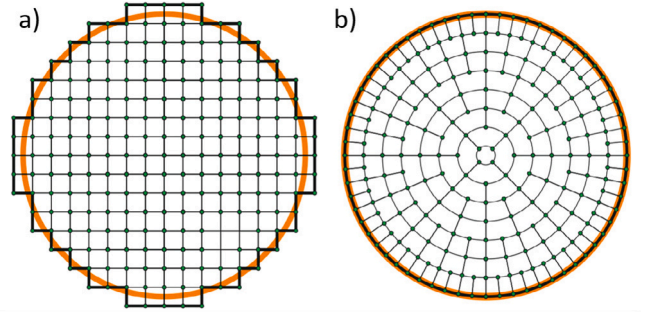

Fig. 2. Sketch of the proposed cylindrical mesh (right) and comparison with the quadrilateral mesh. The main advantage is that the boundary conditions can be much more accurately established in the cylindrical mesh for rounded geometries. However, the magnitudes do not need to be axisymmetric since angular finite differences are allowed within numerical precision. The small green dots are the grid points of our system.

1. Set the number of radial crowns, $N + 1$.
2. Define $\Delta\rho = \frac{R}{N+1/2}$. This will determine the radial step. The radial crowns where we evaluate the functions are indicated by subscript $i = 0, 1, \ldots, N$. The radial positions are $\rho_i = (i + 1/2)\Delta\rho$. At the extremes, $\rho_0 = \frac{1}{2}\Delta\rho$, and $\rho_N = R$.
3. The angular step, $\Delta\varphi_i$, depends on i, which means that the number of points that form each radial crown is different. Set $\Delta\varphi_0 = \frac{\pi}{2}$, which is the maximum angle that satisfies the inequality in the next point
4. Compute $\Delta\varphi_i$, for $0 < i \leq N$, according to

   - If $\delta\Delta\rho > \rho_i \Delta\varphi_{i-1}$, then $\Delta\varphi_i = \Delta\varphi_{i-1}$.
   - If $\delta\Delta\rho \leq \rho_i \Delta\varphi_{i-1}$, then $\Delta\varphi_i = \frac{1}{2}\Delta\varphi_{i-1}$.

   Where we set $\delta = \frac{3}{2}$, so that the error in the radial derivative is of the same order as the error in the angular derivative. The ith radial crown will have L_i angular points uniformly distributed along the crown: $L_i = 2\pi/\Delta\varphi_i$.

Consider an arbitrary function evaluated at a given point, $f(\rho, \varphi)$. Its value at the considered mesh points $(\rho_i, \varphi_j) = ((i + 1/2)\Delta\rho, j\Delta\varphi_i)$, for $i = 0, 1, \ldots, N$ and $j = 0, 1, \ldots, L_i - 1$, would be $f_{i,j}$. Notice that when $i = 0$, $\rho \neq 0$. This is done to avoid the cylindrical coordinates indeterminacy at $\rho = 0$. To evaluate the effective fields [Eqs. (17)–(20)] using the presented mesh, one also needs the discrete derivatives of the (components of) magnetization function. In Fig. 3 one can see the stencils used for evaluating the radial derivatives. The detailed expressions for these discrete radial and angular derivatives are presented in Appendix A.

5. Comparative results between quadrilateral and cylindrical meshes

We have performed the same micromagnetic simulation using two different meshes: one with the QM and the other with the presented CM. The physical process followed is the following: we set $\mathbf{m}(\tau = 0) = \hat{\mathbf{z}}$, and $h_{\text{ext}}(\tau = 0) = 0.4$. Then we let the system evolve as the external field varies from 0.4 to −0.4 following a lineal decay with time, $h_{\text{ext}}(\tau) = 0.4\left(1 - 2\frac{\tau}{T}\right)$, setting $T=6400$, the total simulation time. We choose a radius $R = 7.5$ and $N = 100$, so that $\Delta\rho = \Delta = R/100.5$, being Δ the side of the squared cell in the QM. The time step is set to $\Delta\tau = 5 \cdot 10^{-4}$. The total number of cells are very similar in the QM and in the CM (about 10000 cells, more details in Section 7 and Fig. 7).

We show in Fig. 4 some results for the magnetization obtained during a total simulation time equivalent to 50 ns, comparing the two meshes at different times.
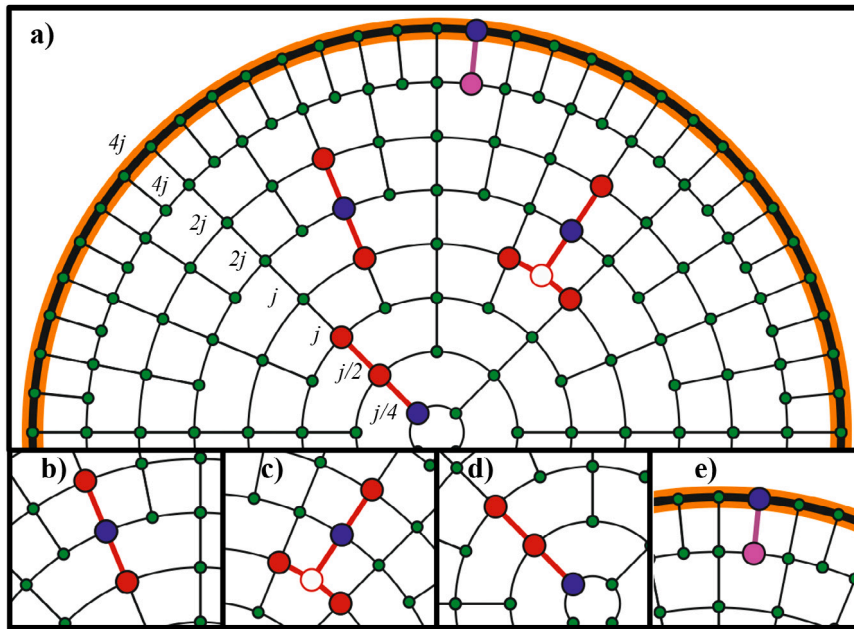
Fig. 3. Sketch for the finite difference of the radial derivatives of a function using the cylindrical mesh. Blue points are where the finite difference is being evaluated, red points are the ones used in the stencil and purple points are the ones where we apply the boundary conditions. In (a) All the possible stencils are sketched, and the relation between the j index of different radial crowns is shown. In (b), (c), and (d) we show the different stencils we can find for $0 < i \leq N$. In (e) we show the points used to apply the boundary conditions.
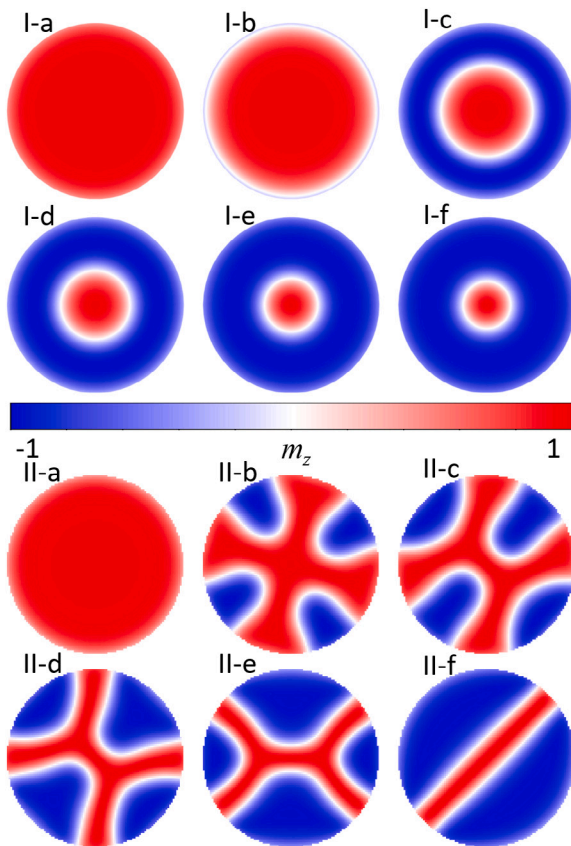

Fig. 4. z-component of the magnetization distribution for an ultra-thin ferromagnetic disk calculated using the cylindrical mesh (I: top-half) and the quadrilateral mesh (II: bottom-half). In each half, each plot corresponds to the different times (a): 0 ns (b): 18.75 ns (c): 25 ns (d): 37.5 ns (e): 46.25 ns, and (f): 50 ns. The central bar is the colorbar for the m_z values.

As seen, using the QM we can find magnetic structures with $\pi/2$ or $\pi/4$ symmetry, while with the CM the axial symmetry is preserved, as should be. It is worth to note that in the QM the $\pi/2$ or $\pi/4$ symmetry appears from the beginning of the calculation. As time goes by, this numerical error becomes more prominent and propagates to the whole sample, triggering the nucleation of a magnetic structure of $\pi/4$ symmetry. Our conclusion is that the cylindrical mesh is more convenient since it offers coherent physical results. Moreover, the computational complexity of the algorithm is similar for both methods (there is approximately the same amount of cells in both methods for the same numerical precision). Although with a finer mesh the numerical error with the QM could be reduced, the computation time needed to have similar numerical error than with the CM would be excessive for a typical simulation.

When reducing the number of cells, reducing the dot size, or/and when there is a relatively large iDMI (affecting considerably the boundary conditions), the use of the presented cylindrical mesh becomes more efficient in terms of accuracy/time.

6. Cylindrical mesh for ferromagnetic rings

Another important advantage of the CM is that it allows to simulate dots with small circular holes, of radius R_0, at their center. If one uses a QM, a cell size much smaller than R_0 is required, yielding prohibitive computational time. With the CM one can simulate these ferromagnetic rings without increasing the computational time since the inner boundary is perfectly fitted regardless the cell size.

Since the $\rho = 0$ point is not in the sample, now the algorithm to generate the mesh, Fig. 5, can be optimized varying slightly the general algorithm presented for non-holed dots. Given a ring with internal and external radii R_0 and R, respectively:

1. Fix the number of radial crowns, $N + 1$.
2. Define $\Delta\rho = \frac{R - R_0}{N}$. This will determine the radial step. The radial crowns are indicated with subscript i. $i = 0, 1, \ldots, N$. The radial position of the crowns where the magnitudes are evaluated are $\rho_i = R_0 + i\Delta\rho$. We have $\rho_0 = R_0$ and $\rho_N = R$.
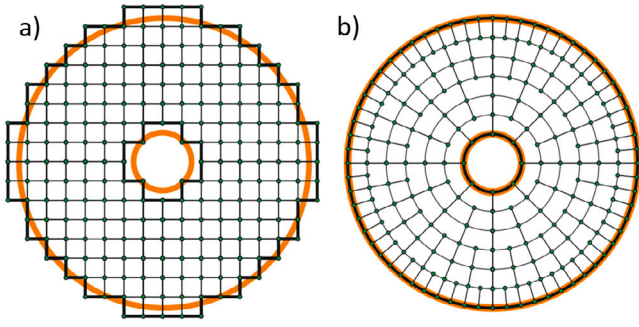
Fig. 5. Sketch of the proposed cylindrical mesh (right) and comparison with the quadrilateral mesh (left), in the case of a ring.

3. The angular step, $\Delta\varphi_i$ will depend on i, which means that the number of cells that form each crown will be different. Set $\Delta\varphi_0 = \frac{2\pi}{2^S}$, being S is the minimum integer that would satisfy the inequality $\frac{3}{2}\Delta\rho \geq \rho_0 \Delta\varphi_0$.

4. Compute $\Delta\varphi_i$ for $i > 0$ using the following relation also with $\delta = \frac{3}{2}$

   - If $\delta\Delta\rho \geq \rho_i \Delta\varphi_{i-1}$, then $\Delta\varphi_i = \Delta\varphi_{i-1}$.
   - If $\delta\Delta\rho < \rho_i \Delta\varphi_{i-1}$, then $\Delta\varphi_i = \frac{1}{2}\Delta\varphi_{i-1}$.

   The ith radial crown has L_i angular points: $L_i = 2\pi/\Delta\varphi_i$

The discrete version of the radial and angular derivatives in this case is detailed in Appendix B.

We repeat the simulation of the previous section but using a ferromagnetic ring with $R = 6$ and $R_0 = 1$. The physical process simulated and the numerical details are exactly the same as in Section 5. The results of the simulations are shown in Fig. 6. Again the differences using the QM and the CM are critical. In particular, we observe that the presence of the hole affects substantially the magnetic structure. In this case the numerical errors in the QM appearing at the central hole are even larger than those at the external border.

7. A particular case: radial mesh

From the previous simulations one may wonder why we have computed the angular derivatives if we are sure that the axial symmetry must be conserved. Actually, if the initial magnetization distribution and the applied field are both cylindrically symmetric, angular derivatives are zero. In this case, the system is actually one dimensional (only ρ dependence) and we could set $\mathbf{m} = 0$ in the cylindrical mesh, resulting in only radial divisions. We call it radial mesh (RM).

In this case $\frac{\partial\mathbf{m}}{\partial\varphi} = 0$, $\frac{\partial^2\mathbf{m}}{\partial^2\varphi} = 0$, and the effective fields are

$$\mathbf{h}_A = \left[\left(\frac{\partial^2 m_\rho}{\partial\rho^2} - \frac{m_\rho}{\rho^2} \right)\hat{\rho} + \left(\frac{\partial^2 m_\varphi}{\partial\rho^2} - \frac{m_\varphi}{\rho^2} \right)\hat{\varphi} + \frac{\partial^2 m_z}{\partial\rho^2}\hat{z} \right], \quad (21)$$

$$\mathbf{h}_D = \xi \left[\frac{1}{\rho}\frac{\partial(\rho m_\rho)}{\partial\rho}\hat{z} - \frac{\partial m_z}{\partial\rho}\hat{\rho} \right], \quad (22)$$

$$\mathbf{h}_K = \kappa\, m_z \hat{z}, \quad (23)$$

The involved functions only depend on ρ. There is no angular dependence, nor angular variations. Thus, the evaluation points would be defined by a single radial index. We use finite differences as we did for the CM, the exact expressions are presented in Appendix C.

For the boundaries, $i = 0, N$; we use the boundary condition, Eq. (10), except for the dot at $i = 0$ where we use $\frac{\partial\mathbf{m}}{\partial\rho}\big|_{\rho=0} = 0$, which must be satisfied if $\mathbf{m}$ is axisymmetric.

Naturally, with this mesh we recover the results obtained in the simulation of the previous section done with the CM, with a substantially less computation time. In Fig. 7, we compare the amount of
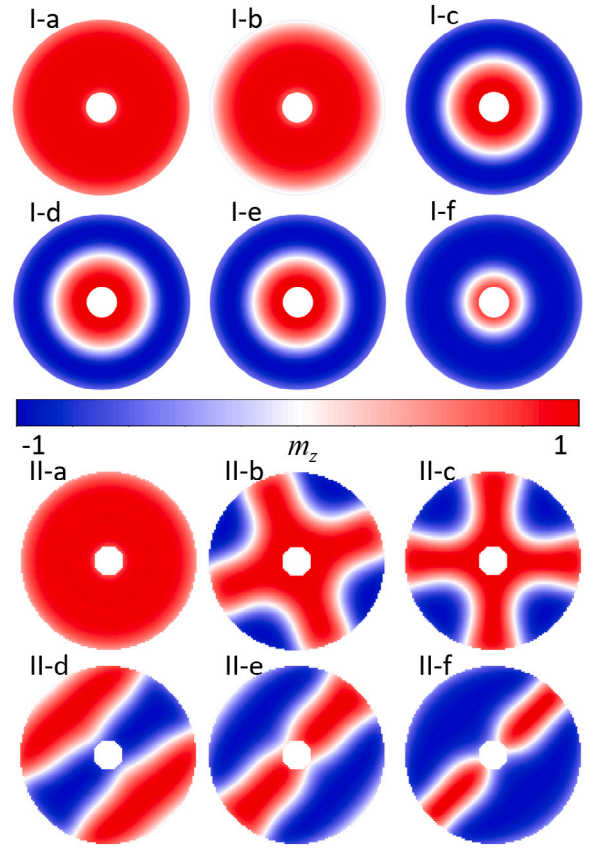

Fig. 6. z-component of the magnetization distribution for a magnetic disk calculated using the cylindrical mesh (I: top-half) and the quadrilateral mesh (II: bottom-half). In each half, each plot correspond to the different times (a): 0 ns (b): 21.25 ns (c): 25 ns (d): 26.25 ns (e): 28.75 ns, and (f): 50 ns . The central bar is the colorbar for the m_z values.

cells that each method (QM, CM and RM) needs to simulate a given ferromagnetic dot. To compare, we plot the total number of cells N_t as a function of the number of radial divisions N_ρ, using $\Delta = \Delta\rho$ for the QM. For a fixed $\Delta\rho$ the horizontal axis is proportional to the radius of the dot. We observe that the amount of cells is always comparable between QM and CM while in the RM the cells used are much less, specially as the radius of the dot increases (with $\Delta\rho$ fixed). Actually, for the RM $N_t \sim R$ while for the QM and the CM $N_t \sim R^2$. As for the computation times, the number of operations needed for each cylindrical is, in average, only slightly larger to those needed for a quadrilateral cell. Actually, in all the simulations the running times for a simulation using the CM is less that 5% larger than that for the QM, with similar number of cells. Note that the RM and the CM do not allow for Fast Fourier Transform algorithms (which are used sometimes to compute demagnetizing fields) since they are not regular meshes.

8. Conclusions

We have presented some studies on magnetic skyrmionic structures, when confined in circular dots or rings. The specially designed CM takes advantage of the axisymmetric boundaries, even though the whole system may not necessarily be axisymmetric. We have seen, by implementing the CM in a typical skyrmionic problem in thin disks, that the use of standard QM can yield numerical error propagation that could invalidate the obtained results. The presented mesh drastically reduces this error, without compromising the computational performance.

A real sample would never be perfectly circular, and one would expect that the real magnetization distribution was not perfectly symmetric. Nevertheless, in simulations, if the symmetry is broken not by
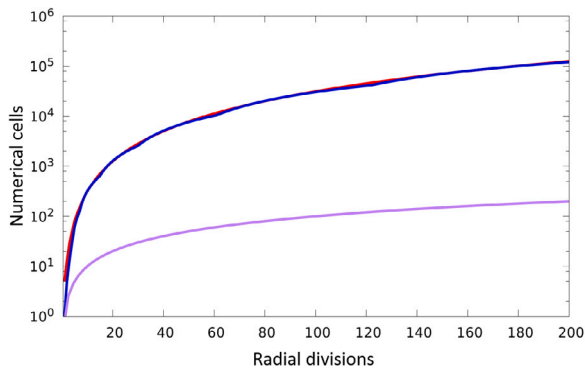
Fig. 7. Number of computational cells as a function of the number of radial divisions for the different meshes used in this work: QM (blue), CM (red), and RM (violet).

controlled notches or defects but as the result of numerical error, this leads to misleading results. We have shown here that these errors can be greatly avoided.

Declaration of competing interest

The authors declare that they have no known competing financial interests or personal relationships that could have appeared to influence the work reported in this paper.

Acknowledgments

Appendix A. Discrete derivatives for the CM mesh

In the case of a circular dot, using the CM mesh, the radial derivatives, when $0 < i < N$, are evaluated as (see the sketches in Fig. 3),

$$\frac{\partial f_{i,j}}{\partial \rho} \simeq \frac{f_{i,j}^+ - f_{i,j}^-}{2\Delta\rho}, \tag{24}$$

$$\frac{\partial^2 f_{i,j}}{\partial \rho^2} \simeq \frac{f_{i,j}^+ - 2f_{i,j} + f_{i,j}^-}{(\Delta\rho)^2}, \tag{25}$$

where the value of $f_{i,j}^+$ and $f_{i,j}^-$ depends on the number of angular divisions of the crowns $i + 1$ and $i - 1$, respectively, according to (in the following $j/2$ is the integer division of j):

- If $\Delta\varphi_{i+1} = \Delta\varphi_i$, then

$$f_{i,j}^+ = f_{i+1,j}, \tag{26}$$

- If $\Delta\varphi_i = \Delta\varphi_{i-1}$, then

$$f_{i,j}^- = f_{i-1,j}. \tag{27}$$

- If $2\Delta\varphi_{i+1} = \Delta\varphi_i$, then

$$f_{i,j}^+ = f_{i+1,2j}. \tag{28}$$

- If $2\Delta\varphi_i = \Delta\varphi_{i-1}$ and j is even, (Fig. 3-b), then

$$f_{i,j}^- = f_{i-1,j/2}. \tag{29}$$

- If $2\Delta\varphi_i = \Delta\varphi_{i-1}$ and j is odd, (Fig. 3-c), then

$$f_{i,j}^- = \frac{1}{2}(f_{i-1,j/2} + f_{i-1,j/2+1}). \tag{30}$$

When $i = 0$, the points $f_{i-1,j}$ do not exist, so we use forward finite differences, (Fig. 3-d),

$$\frac{\partial f_{0,j}}{\partial \rho} \simeq \frac{f_{2,j} - f_{0,j}}{2\Delta\rho}, \tag{31}$$

$$\frac{\partial^2 f_{0,j}}{\partial \rho^2} \simeq \frac{f_{2,j} - 2f_{1,j} + f_{0,j}}{(\Delta\rho)^2}. \tag{32}$$

When $i = N$, the boundary condition of the system, Eq. (10), represented by the purple stencil in (Fig. 3-e), will be used to directly compute the different components of the magnetization, according to:

$$\frac{m_{\rho,N,j} - m_{\rho,N-1,j}}{\Delta\rho} = \frac{\xi}{2} m_{z,N,j}, \tag{33}$$

$$\frac{m_{\varphi,N,j} - m_{\varphi,N-1,j}}{\Delta\rho} = 0, \tag{34}$$

$$\frac{m_{z,N,j} - m_{z,N-1,j}}{\Delta\rho} = -\frac{\xi}{2} m_{\rho,N,j}. \tag{35}$$

The angular derivatives are evaluated taking into account that j is a periodic index, which means that $f_{i,L_i} = f_{i,0}$ and $f_{i,-1} = f_{i,L_i-1}$. Then,

$$\frac{\partial f_{i,j}}{\partial \varphi} \simeq \frac{f_{i,j+1} - f_{i,j-1}}{2\rho_i \Delta\varphi_i}, \tag{36}$$

$$\frac{\partial^2 f_{i,j}}{\partial \varphi^2} \simeq \frac{f_{i,j+1} - 2f_{i,j} + f_{i,j-1}}{(\rho_i \Delta\varphi_i)^2}. \tag{37}$$

Appendix B. Discrete derivatives for the CM mesh in rings

In the case of a ring with the CM mesh, the numerical radial and angular derivatives for $0 < i < N$ are the same Eqs. (31)–(32) (Appendix A). At the boundaries ($i = 0$ and $i = N$) we use the boundary conditions Eq. (10). For $i = N$ we use Eq. (33)–(35) (Appendix A), for $i = 0$ the magnetization is given by

$$\frac{m_{\rho,1,j} - m_{\rho,0,j}}{\Delta\rho} = -\frac{\xi}{2} m_{z,0,j}, \tag{38}$$

$$\frac{m_{\varphi,1,j} - m_{\varphi,0,j}}{\Delta\rho} = 0, \tag{39}$$

$$\frac{m_{z,1,j} - m_{z,0,j}}{\Delta\rho} = \frac{\xi}{2} m_{\rho,0,j}. \tag{40}$$

Appendix C. Discrete derivatives for the RM

Using the same notation as in the CM, the expression used for the first and second radial derivatives are,

$$\frac{\partial f_i}{\partial \rho} \simeq \frac{f_{i+1} - f_{i-1}}{2\Delta\rho} \tag{41}$$

$$\frac{\partial^2 f_i}{\partial \rho^2} \simeq \frac{f_{i+1} - 2f_i + f_{i-1}}{(\Delta\rho)^2} \tag{42}$$

References

[1] H. Kronmuller, M. Fahnle, Micromagnetism and the Microstructure of Ferromagnetic Solids, Cambridge University Press, 2003.

[2] A. Aharoni, Introduction to the Theory of Ferromagnetism, Oxford University Press, 2000.

[3] J. Fidler, T. Schrefl, Micromagnetic modelling - the current state of the art, 2000, http://dx.doi.org/10.1088/0022-3727/33/15/201, https://iopscience.iop.org/article/10.1088/0022-3727/33/15/201/meta.

[4] J. Leliaert, J. Mulkers, Tomorrow's micromagnetic simulations, J. Appl. Phys. 125 (18) (2019) 180901, http://dx.doi.org/10.1063/1.5093730, http://aip.scitation.org/doi/10.1063/1.5093730.

[5] A. Wachowiak, J. Wiebe, M. Bode, O. Pietzsch, M. Morgenstern, R. Wiesendanger, Direct observation of internal spin structure of magnetic vortex cores, Science 298 (5593) (2002) 577–580, http://dx.doi.org/10.1126/science.1075302, https://science.sciencemag.org/content/298/5593/577.abstract.

[6] S. Mangin, D. Ravelosona, J.A. Katine, M.J. Carey, B.D. Terris, E.E. Fullerton, Current-induced magnetization reversal in nanopillars with perpendicular anisotropy, Nature Mater. 5 (3) (2006) 210–215, http://dx.doi.org/10.1038/nmat1595, https://www.nature.com/articles/nmat1595.

[7] B. Van Waeyenberge, A. Puzic, H. Stoll, K.W. Chou, T. Tyliszczak, R. Hertel, M. Fähnle, H. Brückl, K. Rott, G. Reiss, I. Neudecker, D. Weiss, C.H. Back, G. Schütz, Magnetic vortex core reversal by excitation with short bursts of an alternating field, Nature 444 (7118) (2006) 461–464, http://dx.doi.org/10.1038/nature05240, https://www.nature.com/articles/nature05240.

[8] D.E. Nikonov, I.A. Young, Benchmarking spintronic logic devices based on magnetoelectric oxides, 2014, http://dx.doi.org/10.1557/jmr.2014.243, https://link.springer.com/article/10.1557/jmr.2014.243.

[9] S. Luo, M. Song, X. Li, Y. Zhang, J. Hong, X. Yang, X. Zou, N. Xu, L. You, Reconfigurable skyrmion logic gates, Nano Lett. 18 (2) (2018) 1180–1184, http://dx.doi.org/10.1021/acs.nanolett.7b04722, https://pubs.acs.org/doi/abs/10.1021/acs.nanolett.7b04722.

[10] D.E. Heim, J. Tsang, V.S. Speriosu, B.A. Gurney, M.L. Williams, R.E. Fontana, Design and operation of spin valve sensors, IEEE Trans. Magn. 30 (2) (1994) 316–321, http://dx.doi.org/10.1109/20.312279.

[11] D. Suess, A. Bachleitner-Hofmann, A. Satz, H. Weitensfelder, C. Vogler, F. Bruckner, C. Abert, K. Prügl, J. Zimmer, C. Huber, S. Luber, W. Raberg, T. Schrefl, H. Brückl, Topologically protected vortex structures for low-noise magnetic sensors with high linear range, Nat. Electron. 1 (6) (2018) 362–370, http://dx.doi.org/10.1038/s41928-018-0084-2.

[12] R. Tomasello, E. Martinez, R. Zivieri, L. Torres, M. Carpentieri, G. Finocchio, A strategy for the design of skyrmion racetrack memories, Sci. Rep. 4 (2014) 6784, http://dx.doi.org/10.1038/srep06784, http://www.nature.com/srep/2014/141029/srep06784/full/srep06784.html.

[13] J. Iwasaki, W. Koshibae, N. Nagaosa, Colossal spin transfer torque effect on skyrmion along the edge, Nano Lett. 14 (8) (2014) 4432–4437, http://dx.doi.org/10.1021/nl501379k, http://pubs.acs.org/doi/abs/10.1021/nl501379.

[14] A. Thiaville, Y. Nakatani, J. Miltat, Y. Suzuki, Micromagnetic understanding of current-driven domain wall motion in patterned nanowires, Europhys. Lett. (EPL) 69 (6) (2005) 990–996, http://dx.doi.org/10.1209/epl/i2004-10452-6, http://stacks.iop.org/0295-5075/69/i=6/a=990?key=crossref.08cfdeef6135f63254ff9d17d22c1198.

[15] J. Sampaio, V. Cros, S. Rohart, A. Thiaville, A. Fert, Nucleation, stability and current-induced motion of isolated magnetic skyrmions in nanostructures, Nature Nanotechnol. 8 (3) (2013) 839–844, http://dx.doi.org/10.1038/nnano.2013.210.

[16] S. Heinze, K. von Bergmann, M. Menzel, J. Brede, A. Kubetzka, R. Wiesendanger, G. Bihlmayer, S. Blügel, Spontaneous atomic-scale magnetic skyrmion lattice in two dimensions, Nat. Phys. 7 (9) (2011) 713–718, http://dx.doi.org/10.1038/nphys2045, http://www.nature.com/articles/nphys2045.

[17] S. Rohart, A. Thiaville, Skyrmion confinement in ultrathin film nanostructures in the presence of dzyaloshinskii-moriya interaction, Phys. Rev. B 88 (18) (2013) 184422, http://dx.doi.org/10.1103/PhysRevB.88.184422, http://link.aps.org/doi/10.1103/PhysRevB.88.184422.

[18] D. Cortés-Ortuño, N. Romming, M. Beg, K. Von Bergmann, A. Kubetzka, O. Hovorka, H. Fangohr, R. Wiesendanger, Nanoscale magnetic skyrmions and target states in confined geometries, Phys. Rev. B 99 (2019) 214408, http://dx.doi.org/10.1103/PhysRevB.99.214408.

[19] X. Zhang, W. Cai, X. Zhang, Z. Wang, Z. Li, Y. Zhang, K. Cao, N. Lei, W. Kang, Y. Zhang, H. Yu, Y. Zhou, W. Zhao, Skyrmions in magnetic tunnel junctions, ACS Appl. Mater. Interfaces 10 (19) (2018) 16887–16892, http://dx.doi.org/10.1021/ACSAMI.8B03812.

[20] T.L. Gilbert, A phenomenological theory of damping in ferromagnetic materials, IEEE Trans. Magn. 40 (6) (2004) 3443–3449, http://dx.doi.org/10.1109/TMAG.2004.836740.

[21] K.J. Harte, Theory of magnetization ripple in ferromagnetic films, J. Appl. Phys. 39 (3) (1968) 1503–1524, http://dx.doi.org/10.1063/1.1656388, http://aip.scitation.org/doi/10.1063/1.1656388.

[22] J. Castell-Queralt, L. González-Gómez, N. Del-Valle, A. Sanchez, C. Navau, Accelerating, guiding, and compressing skyrmions by defect rails, Nanoscale 11 (26) (2019) 12589–12594, http://dx.doi.org/10.1039/C9NR02171J, http://xlink.rsc.org/?DOI=C9NR02171J.